Electronic supplementary information

Double Enhancement of Hydrogen Storage Capacity of Pd Nanoparticles by 20 at% Replacement with Ir; Systematic Control of Hydrogen Storage in Pd–M Nanoparticles (M = Ir, Pt, Au)

Hirokazu Kobayashi,*[a,b] Miho Yamauchi,[c] Ryuichi Ikeda,[a] Tomokazu Yamamoto,[d,e] Syo Matsumura,[d,e,f] Hiroshi Kitagawa*[a,f,g]

a. Division of Chemistry, Graduate School of Science, Kyoto University, Kitashirakawa-Oiwakecho, Sakyo-ku, Kyoto, 606-8502, Japan.

b. JST, PRESTO, 4-1-8 Honcho, Kawaguchi, Saitama, 332-0012, Japan.

c. International Institute for Carbon-Neutral Energy Research (I2CNER), Kyushu University, 744 Motooka, Nishi-ku, Fukuoka, 819-0395, Japan.

d. Department of Applied Quantum Physics and Nuclear Engineering, Graduate School of Engineering, Kyushu University, Motooka 744, Nishi-ku, Fukuoka, 819-0395, Japan.

e. The Ultramicroscopy Research Center, Kyushu University, Motooka 744, Nishi-ku, Fukuoka, 819-0395, Japan.

f. Inamori Frontier Research Center, Kyushu University, 744 Motooka, Nishi-ku, Fukuoka, 819-0395, Japan.

g. Institute for Integrated Cell-Material Sciences (iCeMS), Kyoto University, Yoshida, Sakyo-ku, Kyoto, 606-8501, Japan.

E-mail: hkobayashi@kuchem.kyoto-u.ac.jp, kitagawa@kuchem.kyoto-u.ac.jp

Table of Contents

1. Experimental details

Synthesis of Pd and Pd/Ir core/shell bimetallic NPs.

First, PVP-protected Pd NPs for the core portion were synthesized by stepwise growth using $PdCl_2$ as a metal precursor. The Pd-core NP (1.7 mmol of Pd) was dispersed in 150 mL of water–ethanol (1:2) mixed solution in a flask equipped with a dropping funnel with an aqueous solution of $IrCl_3 \bullet nH_2O$ (0.425 mmol in 100 mL of water). The reaction flask was connected with a hydrogen balloon, while the funnel was connected with a nitrogen balloon. Air in the reaction flask was replaced with hydrogen first, and the Pd colloid was treated with hydrogen under stirring for 2 h. Then, the aqueous solution of $IrCl_3 \bullet nH_2O$ was added to the reaction system drop by drop over about 4–6 h at 75 °C, and the reaction was continued for another 8 h.

A process of hydrogen adsorption/desorption (PHAD)

The sample of Pd/Ir NPs as prepared was evacuated in vacuo at 373 K for 30–60 min. After evacuation, the sample was exposed to hydrogen gas of 101.3 kPa at 373 K for 30 min, and evacuated at 373 K for 30 min. The PHAD was totally performed three times to form the Pd-Ir solid solution NPs.

Transmission electron microscopy (TEM) images.

TEM images were taken on a JEOL JEM-2000FX operated at 200 kV accelerating voltage. TEM image of the Pd–Ir NPs after the repetition of measurement cycles was taken on a HITACHI HT7700 at an accelerating voltage of 100 kV. For fluid samples, the solution was drop-cast onto a carbon-coated copper grid and allowed to dry at ambient conditions. Solid samples were transferred onto the TEM grid as a heterogeneous dispersion of precipitate in ethanol.

High-angle annular dark-field (HAADF)–STEM and EDX analyses

High-angle annular dark-field (HAADF)–STEM and EDX mapping were recorded on a JEM-ARM 200F STEM instrument operated at 200 kV. The EDX line scanning analysis was taken by a Hitachi HD-2700 operated at 200 kV at the Naka Application Center, Hitachi High-Technologies Corporation.

Synchrotron X-ray powder diffraction (XRD) measurements.

The structures of Pd and Pd–Ir bimetallic NPs were investigated by XRD at BL-1b in KEK-PF. The wavelength was 0.6888284 (1) Å. The XRD patterns of the samples sealed in a glass capillary under vacuum or 86.7 kPa of H_2 gas were measured at 303 K. All of the XRD patterns were obtained with a 0.03° step.

Solid-state ^{2}H NMR measurements.

Solid-state ^{2}H NMR spectra were measured at 303 K with 61.36 MHz frequency using an APOLLO NMR spectrometer (Tecmag). Samples of Pd and Pd–Ir NPs were evacuated in vacuo at 373 K for 30–60 min. After evacuation, the samples were sealed into glass capillaries with 86.7 kPa of $^2H_2$ gas. $^2H_2$ gas in a glass capillary was also prepared for reference.

Pressure-composition-temperature (PCT) apparatus.

The hydrogen absorption–desorption behaviors of Pd and Pd–Ir NPs were measured from 10^{-3} kPa to 100 kPa of hydrogen pressure at 303 K by a volumetric technique using a pressure–composition–temperature (PCT) apparatus (Suzuki Shokan Co., Ltd). 52.7 mg of Pd-Ir NPs and 116.9 mg of Pd NPs were used for PCT measurements.

2. TEM images of Pd and Pd–Ir NPs

TEM images of Pd and Pd–Ir NPs were obtained at an acceleration voltage of 200 kV using a JEOL JEM-2000FX transmission electron microscope. From the TEM images, the mean diameters of the Pd (a) and Pd–Ir NPs before (b) and after (c) the process of hydrogen absorption–desorption (PHAD) were found to be 7.2 ± 1.4, 8.8 ± 1.7, and 9.0 ± 1.8 nm, respectively. In comparison with the mean diameter of Pd–Ir NPs before the PHAD, the diameter of Pd–Ir NPs did not change after the PHAD, showing that aggregation of particles is not promoted by the PHAD.

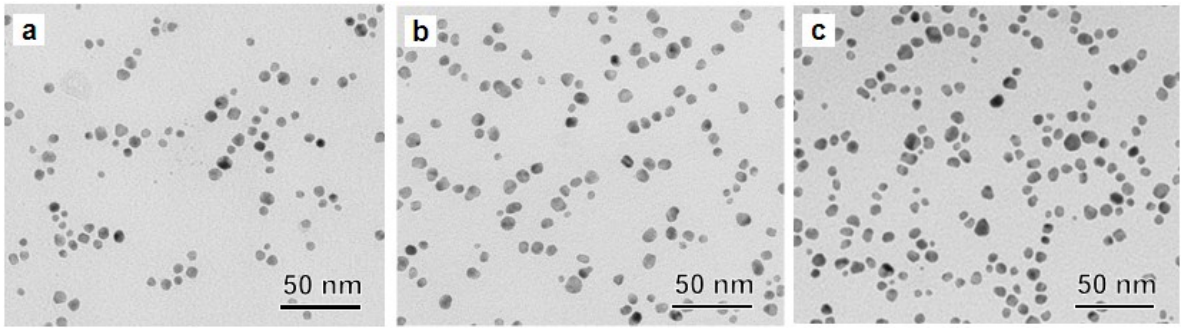

Figure S1. TEM images of (a) Pd and Pd–Ir NPs (b) before and (c) after the PHAD at 373 K.

3. XRD patterns of Pd and Pd/Ir NPs

The structures of Pd and Pd/Ir bimetallic NPs were investigated by XRD using synchrotron radiation of 68.88 pm wavelength at the beam line BL-1b in KEK-PF. The XRD patterns of the sample sealed in a glass capillary were measured at 303 K. Figure S2 shows the powder XRD patterns of as-prepared Pd and Pd/Ir NPs. Pd NPs showed a diffraction pattern from a face-centered-cubic (fcc) lattice. On the other hand, the diffraction pattern of Pd/Ir NPs was significantly different from that of Pd NPs; that is, another fcc component was observed at the higher-angle side of each peak from the Pd lattice. The emergence of a new diffraction component suggests that an Ir shell with fcc symmetry is formed on the Pd core.

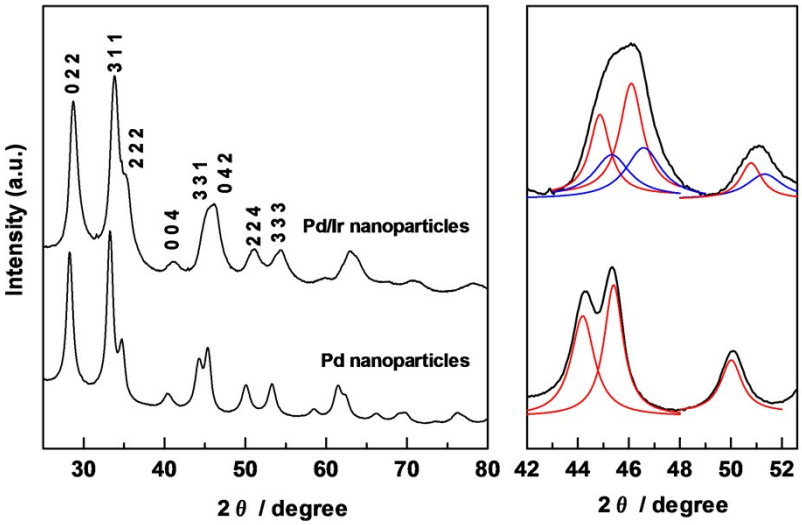

Figure S2. Powder XRD patterns of Pd and Pd/Ir NPs. Red and blue lines show fitting curves of Pd and Ir components, respectively.

4. Line-scanning profiles of Ir (blue) and Pd (green) across Pd-Ir solid-solution NP

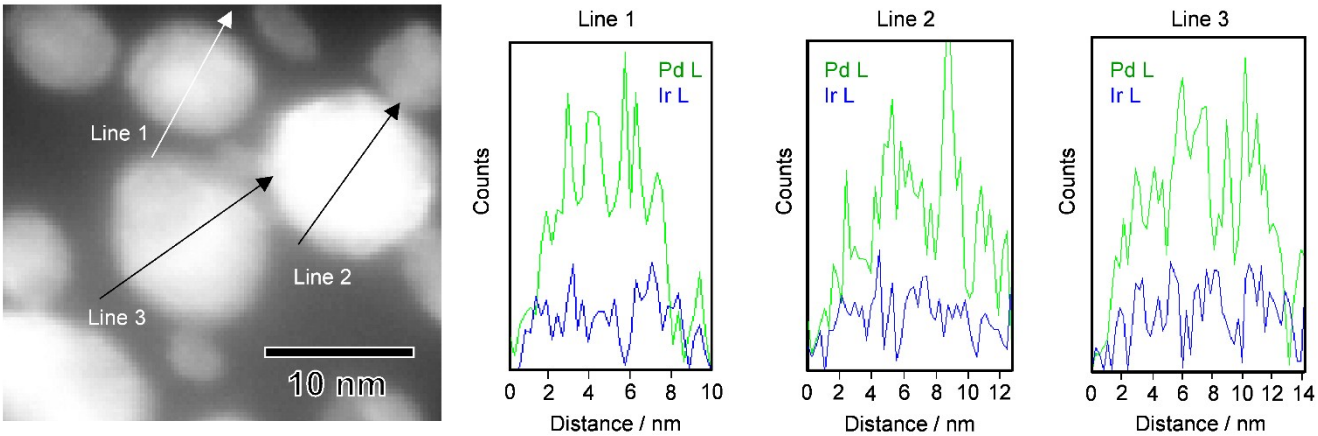

Figure S3. Line-scanning profiles of Ir (blue) and Pd (green) across Pd-Ir solid-solution NP

5. XRD patterns of Pd-Ir NPs before/after the PHAD

Figure S4 shows powder XRD patterns of Pd–Ir NPs (a) before and (b) after the PHAD. The diffraction patterns, which consist of core Pd and shell Ir portions, changed to a single fcc lattice after the PHAD, indicating that the initial core/shell-type structure was altered to a solid-solution-type structure.

.

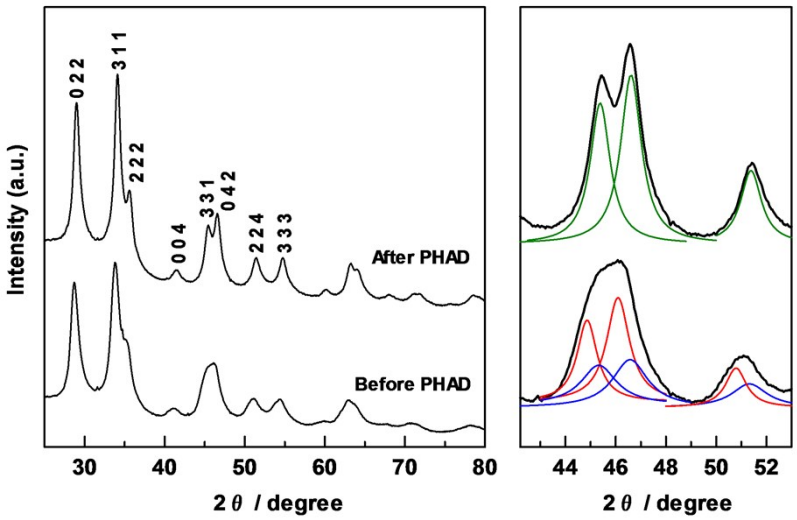

Figure S4. Powder XRD patterns of Pd–Ir NPs before/after the PHAD. Red and blue lines show fitting curves of Pd and Ir components, respectively. The green line shows a fitting curve of Pd–Ir solid-solution alloy component.

6. Solid-state ^{2}H NMR spectra

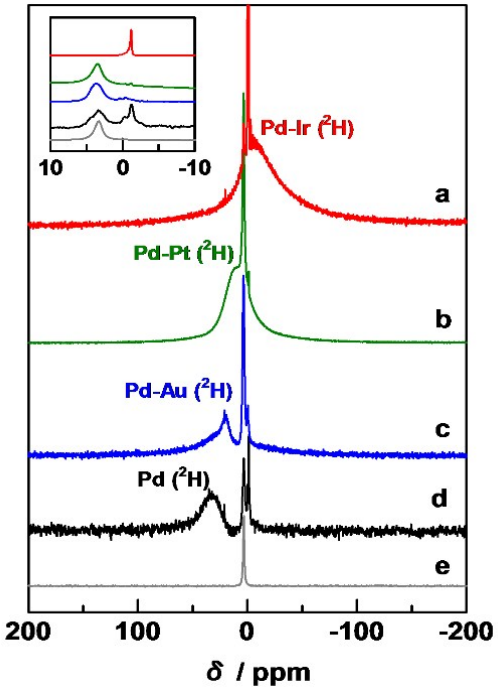

Figure S5. Solid-state ^{2}H NMR spectra for the samples of Pd–Ir NPs after the PHAD (a). The samples of Pd–Pt (b) and Pd–Au (c) solid-solution NPs, Pd (d) and $^2H_2$ gas (e) were also measured for reference. All samples were measured under 86.7 kPa of $^2H_2$ gas at 303 K.

7. PC isotherms

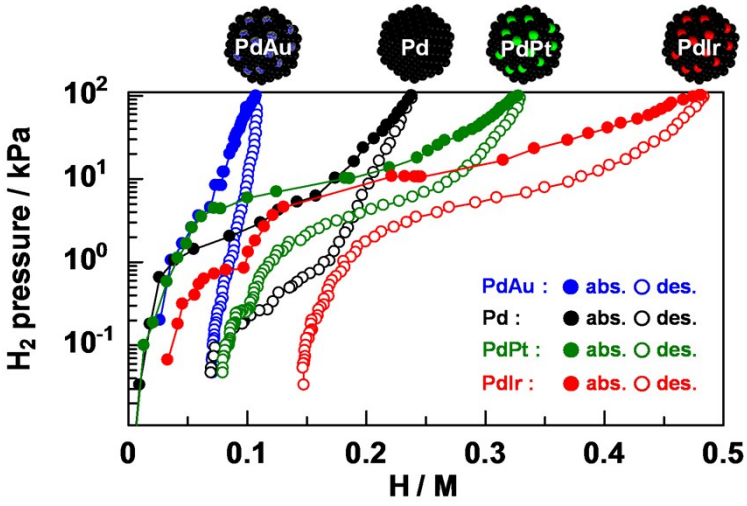

Figure S6. PC isotherms of Pd, Pd_{80}–Au_{20}, Pd_{79}–Pt_{21}, and Pd_{80}–Ir_{20} solid-solution NPs at 303 K.

8. Temperature dependency of PC isotherms for Pd NPs

As shown in Figure S7, the hydrogen concentration increased with decreasing measurement temperature, indicating that hydrogen-storage processes involve an exothermic reaction between Pd NPs and hydrogen atoms. The temperature dependence of the plateau pressure of the absorption isotherms was examined at a hydrogen concentration of H/M = 0.15. From the van't Hoff plots of H_2, the enthalpy $-\Delta H_{\alpha\rightarrow\beta}$ and entropy $\Delta S_{\alpha\rightarrow\beta}$ changes were estimated to be –18.6 kJ $(H_2\ mol)^{-1}$ and –36 J $(H_2\ mol)^{-1}\ K^{-1}$, respectively.

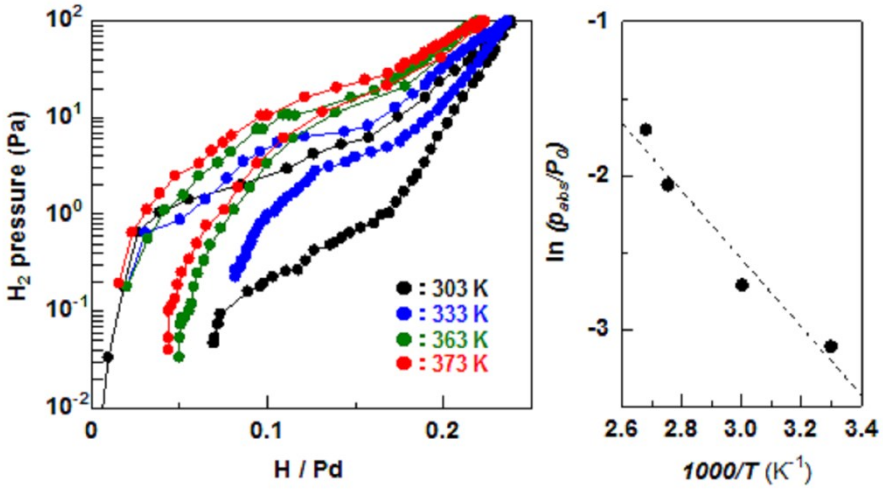

Figure S7. Temperature dependence of PC isotherms and absorption van't Hoff plot for Pd NPs.

9. Temperature dependency of PC isotherms for Pd-Au NPs

As shown in Figure S8, the hydrogen concentration increased with decreasing measurement temperature, indicating that hydrogen-storage processes involve an exothermic reaction between Pd–Au NPs and hydrogen atoms. The temperature dependence of the plateau pressure of the absorption isotherms was examined at a hydrogen concentration of H/M = 0.05. From the van't Hoff plots of H_2, the enthalpy $-\Delta H_{\alpha\rightarrow\beta}$ and entropy $\Delta S_{\alpha\rightarrow\beta}$ changes were estimated to be –3.5 kJ $(H_2\ mol)^{-1}$ and –15 J $(H_2\ mol)^{-1}\ K^{-1}$, respectively.

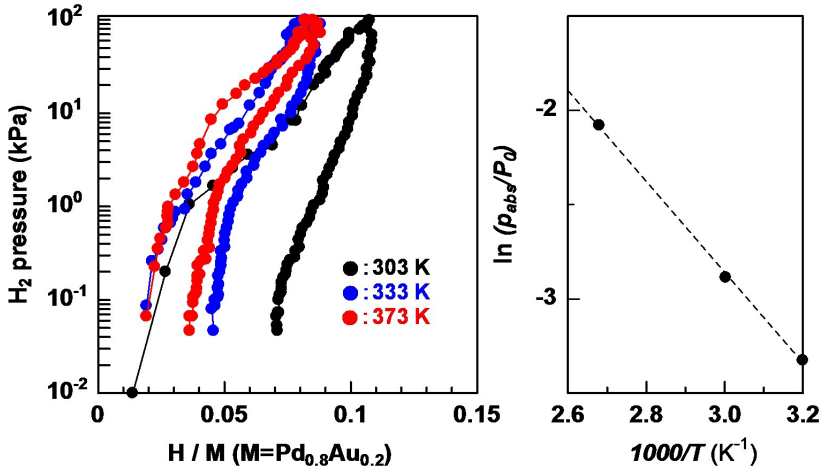

Figure S8. Temperature dependence of PC isotherms and absorption van't Hoff plot for Pd–Au NPs.

10. Temperature dependency of PC isotherms for Pd-Pt NPs

As shown in Figure S9, the hydrogen concentration increased with decreasing measurement temperature, indicating that hydrogen-storage processes involve an exothermic reaction between Pd–Pt NPs and hydrogen atoms. The temperature dependence of the plateau pressure of the absorption isotherms was examined at a hydrogen concentration of H/M = 0.175. From the van't Hoff plots of H_2, the enthalpy $-\Delta H_{\alpha\rightarrow\beta}$ and entropy $\Delta S_{\alpha\rightarrow\beta}$ changes were estimated to be –25.0 kJ $(H_2\ mol)^{-1}$ and –63 J $(H_2\ mol)^{-1}\ K^{-1}$, respectively.

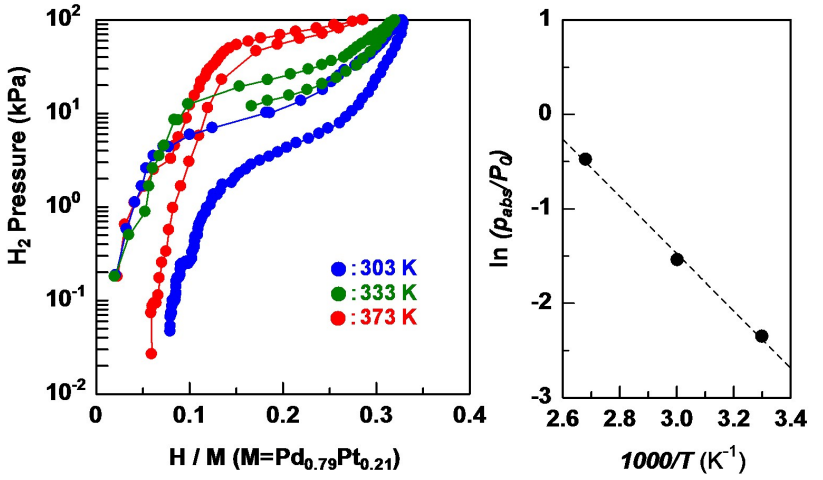

Figure S9. Temperature dependence of PC isotherms and absorption van't Hoff plot for Pd–Pt NPs.

11. Calculation of enthalpy values from van't Hoff plots for Pd, Pd-Au, Pd-Pt and Pd-Ir NPs

In PC isotherms of Pd, Pd-Au, Pd-Pt and Pd-Ir NPs, the plateau pressures are unclear due to the nanosize, which makes us difficult to estimate values for the enthalpy using van't Hoff plots. Therefore, we consider the plateau pressures at several points of H/M, and enthalpy values were calculated at each point from the van't Hoff plots shown in Figure S10. The maximum values are used as the enthalpy value in this paper.

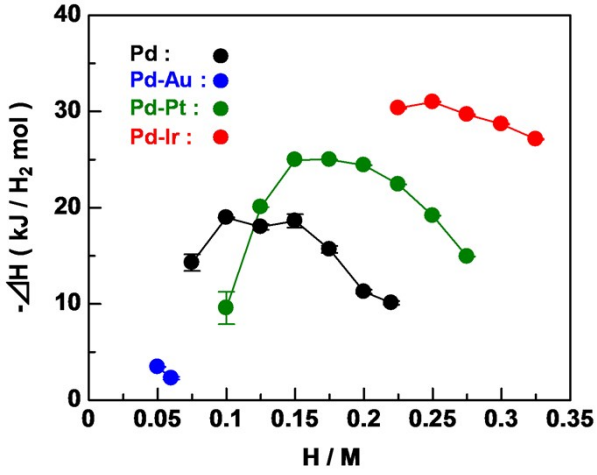

Figure S10. Values for the enthalpy estimated by van't Hoff plot at several points of H/M

12. Absorption van't Hoff plots

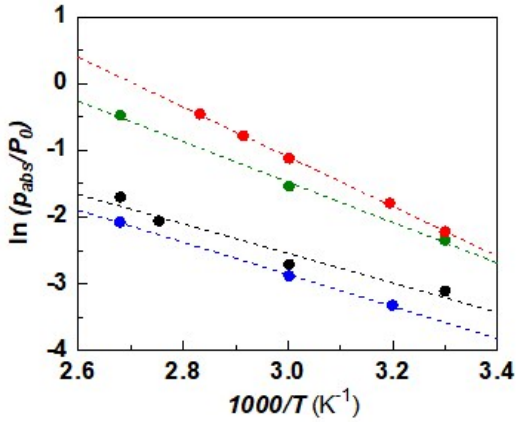

	$-\Delta H_{\alpha\rightarrow\beta}$ kJ $(H_2\ mol)^{-1}$	$\Delta S_{\alpha\rightarrow\beta}$ J $(H_2\ mol)^{-1}\ K^{-1}$
Pd	-18.6(7)	-36(1)
Pd-Au	-3.5(0)	-15(0)
Pd-Pt	-25.0(0)	-63(0)
Pd-Ir	-31.0(0)	-84(0)

Figure S11. Absorption van't Hoff plots and the enthalpy $-\Delta H_{\alpha\rightarrow\beta}$ and entropy $\Delta S_{\alpha\rightarrow\beta}$ changes for Pd NPs and Pd-based solid-solution alloy NPs.

13. PC isotherm and TEM image after the measurements of temperature-dependent PC isotherms of Pd–Ir solid-solution NPs

After the measurements of temperature-dependent PC isotherms of Pd–Ir solid-solution NPs, the total amount of hydrogen absorbed at 101.3 kPa was 0.47 $H/Pd_{0.8}Ir_{0.2}$, which is in good agreement with that of the as-prepared Pd-Ir solid-solution NPs (0.48 $H/Pd_{0.8}Ir_{0.2}$). From the TEM image, the mean diameter of the Pd–Ir NPs after the repetition of measurement cycles was found to be 8.7 ± 1.9 nm, which is consistent with that of the as-prepared Pd-Ir solid-solution NPs (9.0 ± 1.8 nm).

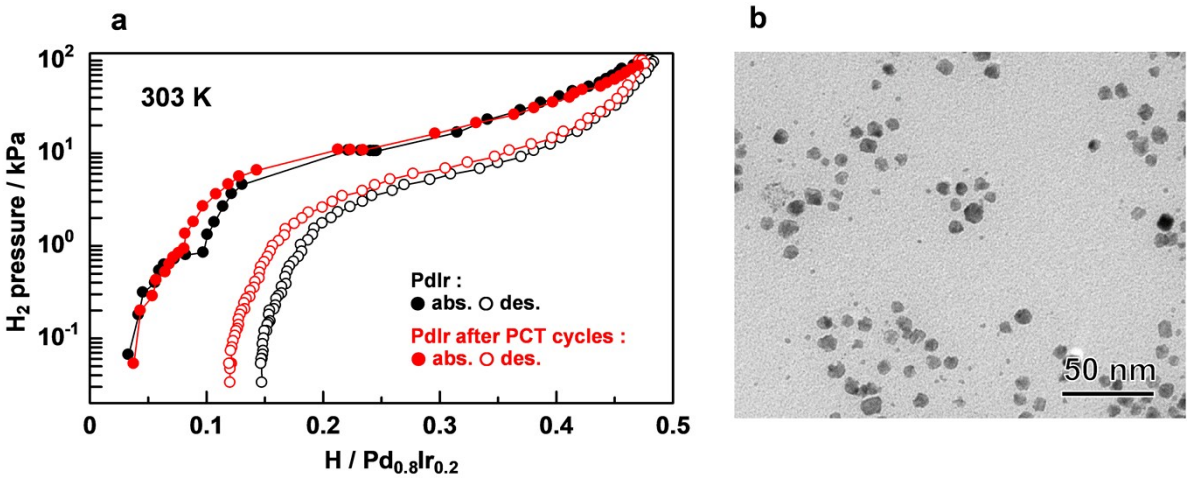

Figure S12. a. PC isotherm and **b.** TEM image after the measurements of temperature-dependent PC isotherms of the Pd–Ir solid-solution NPs.

14. Author Contributions

H. Kitagawa and H. Kobayashi designed this study. H. Kobayashi performed the experiments. M. Yamauchi and R. Ikeda assisted with the synchrotron PXRD and solid-state ^2H NMR measurements. T. Yamamoto and S. Matsumura conducted the high-angle annular dark-field STEM and EDX mapping. All authors contributed to the manuscript.